DOI: 10.1002/chem.200700499

Optical Nanosensor Design with Uniform Pore Geometry and Large Particle Morphology

Sherif A. El-Safty,* Adel A. Ismail, Hideyuki Matsunaga, and Fujio Mizukami[a]

Abstract: Appropriate design of nanosensors for optically selective, sensitive sensing systems is needed for naked-eye detection of pollutants for environmental cleanup of toxic heavy-metal ions. Mesostructured materials with two- or three-dimensional (2D or 3D) geometries and large particle morphologies show promise as probe carriers, and can therefore be used to reproducibly fabricate uniformly packed nanosensors. This is the first report on the effects of significant key properties of the mesostructured carriers, such as morphology, geometry, and pore shape, on the functionality of optical nanosensor designs. Such mesostructured sensors with superior physical characteristics can be used as components in sensing systems with excellent stability and sensitivity, and with rapid detection response. The nanosensor design can enhance the selectivity even at low concentrations of the pollutant target ions (nanomolar level). Among the nanosensors developed here, the large pore-surface grains of highly ordered 3D monoliths (HOM) exhibited a high adsorption capability of the Pyrogallol Red probe and high accessibility to analyte ion transport, leading to possible naked-eye detection of Sb^{III} ions at concentrations as low as 10^{-9} mol dm^{-3} and at a wide detection range of 0.5 ppb to 3 ppm. A key finding in our study was that our mesostructured nanosensor designs retained highly efficient sensitivity without a significant increase in kinetic hindrance, despite the slight decrease of the specific activity of the electron acceptor/donor strength of the probe functional group after several regeneration/reuse cycles. The results, in general, indicate that large-scale reversibility of optical nanosensors is feasible in such metal-ion sensing systems.

Keywords: antimony · mesoporous materials · nanostructures · sensors · toxic ions

Introduction

The detection, or "sensing", of toxic pollutants is a most intriguing development at the nanoscale level.[1] Chemical surface functionalization of ordered nanoscale structures can be used to produce materials that have desired surface properties for applications such as sensing, catalysis, separation, and nanoreactors.[2,3] Considerable attention has been focused on tailoring the chemical composition of mesoporous materials by using host probe molecules, leading to the design of molecular receptors as "chemical sensors" that can convert their chemical information into analytically useful signals upon binding to specific guests.[1–3] In general, conventional treatment methods involving these chemical sensors have attracted much interest due to their potential ease of detection and quantification of pollutants in widespread applications, such as waste management, environmental cleanup chemistry, and clinical toxicology.[1,4] Among all sensing techniques, optical sensors are the most effective due to their accurate detection of pollutants at low concentrations without control of the experimental environment or the use of fairly sophisticated equipment.[1–3] The key components in this sensing method are optical sensors that can efficiently detect toxic ions in terms of sensitivity and selectivity with real-time monitoring.[5,6] Such features are currently required to analyze today's ultratrace levels of environmental pollutants.[7,8] The development of sensing processes entails invention, optimization, and commercialization, and remains a significant challenge in materials science.[9–11]

Recently, the design of optical sensors based on mesoporous materials as promising detectors for pollutant species

---

[a] Dr. S. A. El-Safty, Dr. A. A. Ismail, Dr. H. Matsunaga,
Dr. F. Mizukami
Research Center for Compact Chemical Process (CCP)
National Institute of Advanced Industrial Science & Technology
(AIST)
4-2-1 Nigatake, Miyagino-ku, Sendai 983-8551 (Japan)
Fax: (+81) 22-237-5226
E-mail: sherif.el-safty@aist.go.jp

Supporting information for this article is available on the WWW under http://www.chemeurj.org/ or from the author.

has attracted much attention in the field of environmental analysis.[12,13] The development of these mesostructures as carriers is a key to defined sensing systems in environmental cleanup and pollutant recovery.[14–18] In this respect, the introduction of coupling agents, such as thiol ligands, onto the surface of hexagonal MCM-41 silica supports led to the creation of a new kind of chemical adsorbent that is extremely efficient in removing mercury and other heavy-metal ions.[19] With the expectation of developing higher-efficiency nanosensors, the challenges that remain for these nanofabricated sensors include controlled immobilization of probe moieties in the support matrices and a stable, reproducible sensor response after multiple reuse cycles.[14–20] More recent developments include optical nanosensors, which led to the highly reliable detection of toxic ions by utilizing three-dimensional (3D) nanoscale cagelike structures.[20] These cage nanosensors show promise as probe sinks with high metal-ion fluxes across the surface grains composed of large-particle monoliths.[20]

Due to their high toxicity, antimony and its compounds are considered by the United States Environmental Protection Agency (USEPA) and the European Union Council of the European Communities to be priority pollutants. Typically, the USEPA recommends that drinking water contains less than 6 ppb of antimony. However, the maximum contaminant level could be substantially elevated to 100 ppb concentration in the proximity of anthropogenic sources.[21] The Sb^{III} oxidation state of antimony is considerably more toxic and mobile than Sb^{V}. The chemical form of its compounds strongly influences toxicity.[21] Antimony is produced by the metallurgical, alloy, and rubber industries, and has also been found in geological, biological, and water samples as a result of various anthropogenic activities.[22] As antimony-containing additives are used in brake linings and tire vulcanization processes, road traffic is also a significant source of pollution.[23] There is a demand for accurate and specific determination of trace concentrations of Sb^{III} ions. Several methods to determine the preconcentration and separation of Sb^{III} ions have been developed in the past few decades, such as spectrophotometry, ion exchange, chelating adsorbents and coprecipitation,[24] inductively coupled plasma mass spectrometry (ICP-MS), inductively coupled plasma optical-emission spectroscopy (ICP-OES),[25a,b] voltammetry,[25c,d] atomic-absorption spectrometry (AAS),[26] and chromatographic and fluorimetric detection approaches.[27] Although these techniques are the most useful sensitive approaches for detecting Sb^{III} ions, they all have limitations, such as requiring sophisticated pieces of equipment or extreme control of experiments and their environment, thus leading to a time-consuming response and high operating costs. In this respect, determination of trace concentrations of toxic Sb^{III} ions with increased selectivity, response speed, and sensitivity is urgently needed. To the best of our knowledge, a nanosensor based on hexagonally and cubically ordered mesoporous silica monoliths (highly ordered monolith (HOM) type) could detect Sb^{III} ions with sufficient efficiency to exceed the drinking water standards recommended by the USEPA.

Here, we report the key factors in the design of optical nanosensors for efficient sensing of toxic metal ions down to subnanomolar concentrations with rapid response times (on the order of seconds). Although optical sensors based on large, cagelike sinks are used for visual detection of Sb^{III} ions, as previously reported,[20] the current work revealed the first evidence of the advantages of nanoscale pore geometry and shape and the particle morphology of the mesostructured probe carriers in expanding the applicability of optical nanosensors for sensitive and selective discrimination of trace levels of toxic analytes, such as Sb^{III} ions. The key to achieving such a practical nanosensor is the control of the nanosensor design and the experimental sensing conditions. Pyrogallol Red (PR)-based nanosensors led to the creation of possible naked-eye detection of Sb^{III} ions at a concentration as low as 10^{-9} mol dm^{3} and over a wide detection range of 0.5 ppb to 3 ppm. Among all probe carriers, the HOMs with 3D cagelike geometry led to high Sb^{III}-ion loading capability and to strong binding affinity even at low concentrations of Sb^{III} target ions. Significantly, the nanosensors showed unprecedented retention of the potential naked-eye sensing functionality, even after long-term storage and after several regeneration/reuse cycles.

Results and Discussion

Design of 2D and 3D optical nanosensors: Control over the periodicity, morphology, and uniformly sized pore shapes of the mesostructure was clearly revealed by the fabricated 2D hexagonal *P6mm* and 3D cubic *Pm*3*n* geometries (see Supporting Information S1 and S2).[28–30] In this work, these mesostructures show promise as carriers in the design of optical nanosensors. The immobilization of the PR chromophore into 2D and 3D mesopore geometries led to the creation of optical chemical nanosensors that have efficient sensing functionalities (Scheme 1). As a result of the potential leaching of the hydrophilic PR chromophore by the washing cycle, the PR probe could not be directly embedded on the silica surface matrices without tuning the surface polarity. Optical nanosensors were successfully fabricated with the PR probe by using a silica-modified *N*-trimethoxysilylpropyl-*N*,*N*,*N*-trimethylammonium chloride (TMAC) coupling agent (Scheme 1).[14–19]

Post-grafting techniques can be used to create highly tuned, functional nanostructured surfaces, which can act as positively charged carriers. Thermogravimetric analysis–differential thermal analysis (TGA-DTA) and Fourier-transform IR (FTIR) spectroscopy provided evidence of the TMAC-modified free-standing silica supports (see the Supporting Information S3 and S4).[31–33] With the introduction of PR probe molecules, strong ionic interactions successfully occurred between the PR chromophore containing a sulfonate acid group and the carriers charged by the functionalized ammonium ion (Scheme 1). In addition, the hydrogen

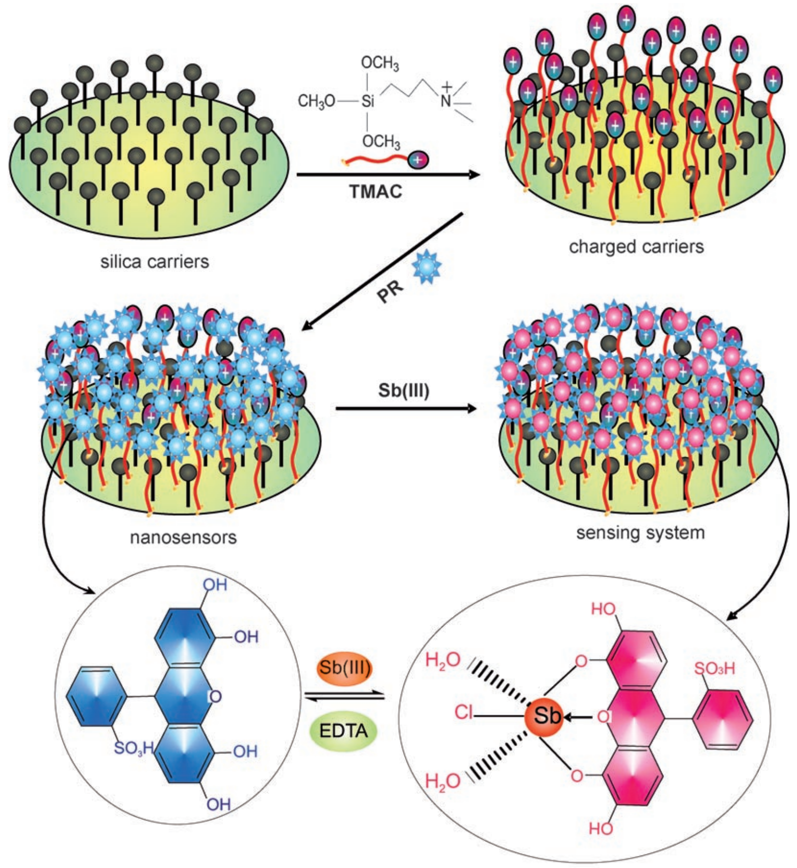

Scheme 1. Systematic design of optical chemical nanosensors through the surface functionalization of ordered nanoscale structures by a TMAC ligand and PR probe chromophore. The formation of the [Sb–PR]$^+$ complex during the sensing recognition of Sb^{III} ions by optical nanosensors and the possible reversibility of the process by using ethylenediaminetetratacetic acid (EDTA) as a stripping agent.

bonding between the PR molecules and Si–OH surfaces could also induce retention of the incorporated PR probe during the washing cycle, indicating the successful design of optical nanosensors. ^{29}Si NMR spectroscopy indicated successful tuning of the silica surfaces by charged molecules (TMAC) and by a probe moiety (PR) through clarification of the molecular environment in the silica materials (see the Supporting Information S5).[34,35] The TMAC-functionalized mesoporous materials, in principle, not only led to strongly bound PR molecules on the pore surfaces, but also enhanced the loading amount and accessibility of the PR probe. One of the most exciting aspects of this chemical nanosensor design is that the PR chromophore moieties can be embedded in the pore matrices without significant alteration of the mesostructured regularity, particle morphology, or pore geometry of 2D and 3D materials. This developed design yielded a sensing response in the chemical nanosensors that was generally linear, as revealed by the high selectivity and sensitivity for Sb^{III} target ions and the rapid response time (Scheme 1).

Uniformly sized and geometrically controlled nanosensors: Transmission electron microscopy (TEM) images (Figure 1A,B) reveal well-organized mesopore arrays over a large area of the hexagonal *P6mm* and cubic *Pm*3*n* lattices, despite the severe synthesis conditions during the grafting process of TMAC and the loading coverage of bulky chromophore molecules, such as the PR probe. The TEM image in Figure 1A shows a uniformly sized pore arrangement and continuous hexagonal arrays along all directions of the functionalized TMAC–silica and nanosensors.[28,29] Furthermore, the image in Figure 1B reveals a spherical arrangement with crystal orientations running along the [111] direction (with slight defects, as shown by arrows), indicating that the cubic morphology of these nanosensors is primitive face-centered cubic with a *Pm*3*n* space group.[36]

The X-ray diffraction (XRD) profiles (Figure 1C) provide evidence that the ordered hexagonal and cubic structures were characteristic of the fabricated nanosensors.[28–30] Despite the high loading level of the organic moieties into the necked pore channels or on the pore surface, finely resolved Bragg diffraction peaks were clearly evident for the hexagonal and cubic nanosensor geometries. This finding indicates that the electrostatic interaction between the modified silica–TMAC and the PR molecules (Scheme 1) was sufficient to dope the hydrophilic chromophore probe (PR) into rigid condensed framework matrices while retaining the mesoscopically orientational order (see the Supporting Information S2). These rigid matrices with such order led to high flux and transport of analyte ions during the detection process.

The N_2 isotherms revealed the uniformity and regularity of the 2D and 3D nanosensors, as evidenced from a well-known sharp inflection of adsorption/desorption branches (Figure 1D). With hexagonal nanosensors, the isotherms showed a pronounced H_1-type hysteresis loop with the SBA-15 sample, indicating an increase in the open cylindrical pore size (Figure 1Da,b).[37] In turn, this H_2-type hysteresis loop and well-defined steepness of isotherms (Figure 1Dc) indicated that uniform cagelike pore structures were characteristic of the cubic *Pm*3*n* nanosensors.[36,38,39] The adsorp-

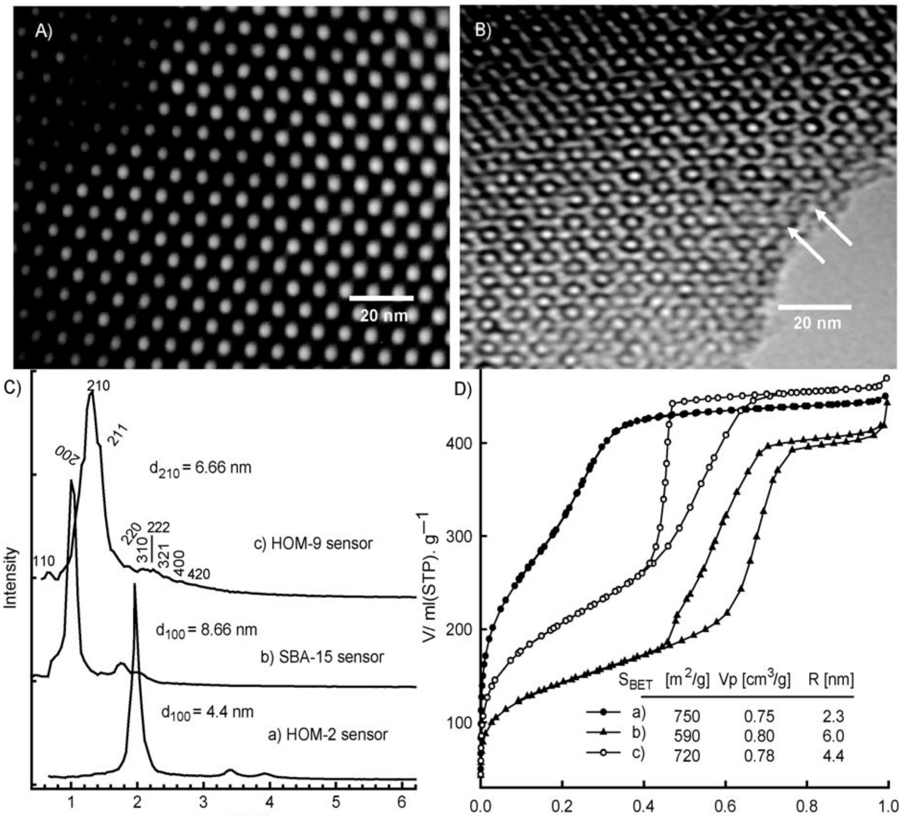

Figure 1. Representative TEM images of A) uniformly shaped hexagonal SBA-15/TMAC/PR nanosensors and B) cage cubic *Pm*3*n* monolithic HOM-9/TMAC/PR nanosensors recorded along the [111] direction. C) XRD patterns and D) N_2 adsorption/desorption isotherms at 77 K of HOM-2/TMAC/PR (a), SBA-15/TMAC/PR (b), and HOM-9/TMAC/PR (c) nanosensors. *V*: volume, P/P_0: relative pressure, S_{BET}: Brunauer–Emmett–Teller (BET) surface area, V_p: pore volume; *R*: pore size.

tion branches were significantly shifted to lower relative pressure (P/P_0) when the TMAC ligand and PR probe were embedded (Figure 1D and S2 in the Supporting Information), indicating the inclusion of the organic moieties, to some extent, into the mesopore without a significant effect on the uniformly sized structures. Further evidence of this inclusion inside the pore was that, first, the width of the hysteresis loop decreased with embedding of the organic moieties, indicating a decrease in the nanoscale pore size with all of the fabricated nanosensors. Second, a decrease in the surface area and pore volume with the functionalization of hexagonal and cubic nanosensors provided further evidence that the organic moieties were embedded inside the mesopore (see the Supporting Information Table S2). Such embedding in the pore does not exclude the possible coexistence of the functionalized moieties on the outer pore surfaces of materials. However, although the large-particle HOM-2 monoliths had smaller pore sizes (≈3 nm) than the SBA-15 materials (Table S2), HOM-2 showed a higher level of adsorption (*Q*) of the probe molecules (Table 1), indicating the effectiveness of the outer-surface modification of the large-particle morphology in such an immobilization process. The retention of the physical characteristics of nanosensors, such as pore size, volume, and surface area (Figure 1D, insert), led to ligand-binding affinity with metal ions during the detection process, indicating a

Table 1. The efficiency of optical sensing systems in terms of accessibility, sensitivity, stability, kinetic response, and reversibility features[a] during the naked-eye detection of toxic Sb^{III} ions by using nanostructured sensors.

Sensor structures	*Q* [mmol g^{-1}]	$10^9 \times$ LOD [mol dm^{-3}]	D_R [mol dm^{-3}]	R_t [s]	Stability [months]	Sensor featured with reuse cycles				
						No.	R_t [min]	S_{BET} [m^{2}g^{-1}]	V_p [cm^{3}g^{-1}]	*E* [%]
hexagonal SBA-15 powder	0.021	20.9	4.1×10^{-8} to 1.621×10^{-5}	240	4	1	6	550	0.75	85
						2	8	520	0.71	79
						3	10	490	0.67	70
hexagonal HOM-2 monoliths	0.025	3.73	8.2×10^{-9} to 1.62×10^{-5}	60	8	1	2	700	0.71	95
						2	3	670	0.72	90
						3	6	600	0.68	80
cubic *Pm*3*n* HOM-9 monoliths	0.03	1.36	4.1×10^{-9} to 2.05×10^{-5}	45	12	1	1	700	0.75	97
						2	2	670	0.72	91
						3	4	620	0.68	86

[a] Adsorption amounts (*Q*) of the PR probe, detection limit (LOD), and range (D_R), kinetic response time (R_t), and the efficiency of the sensing design (*E*) after several (No.) regeneration cycles.

wide, tunable detection range for analyte ions (Table 1).[40–42] In addition, homogeneous diffusion and rapid transport of analyte ions onto the ordered pore networks of materials led to excellent sensitivity with rapid response times of detection (Table 1).[18–20]

Optically nanostructured sensor systems: The effect of pore geometry and shape and particle morphology on the improved recognition of metal ions was investigated by using fabricated hexagonal and cubic nanosensors to detect Sb^{III} ions. Although the selectivity for Sb^{III} ions was not affected by the physical characteristics of the nanosensrs, the strength of this Sb^{III} sensing system in terms of sensitivity and response-time detection was significantly affected by the particle morphology and pore shape and geometry of the nanosensors (Figure 2 and Table 1).

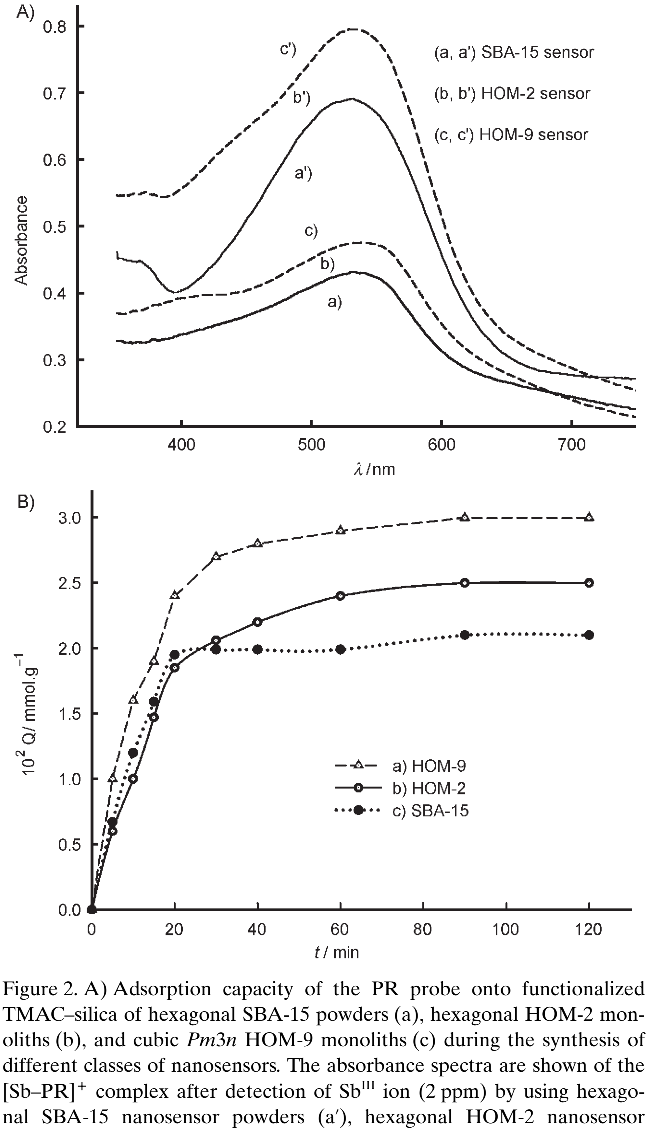

Figure 2. A) Adsorption capacity of the PR probe onto functionalized TMAC–silica of hexagonal SBA-15 powders (a), hexagonal HOM-2 monoliths (b), and cubic *Pm*3*n* HOM-9 monoliths (c) during the synthesis of different classes of nanosensors. The absorbance spectra are shown of the $[Sb–PR]^+$ complex after detection of Sb^{III} ion (2 ppm) by using hexagonal SBA-15 nanosensor powders (a′), hexagonal HOM-2 nanosensor monoliths (b′), and cubic *Pm*3*n* HOM-9 nanosensor monoliths (c′). B) Kinetic time-dependence studies of the PR-probe adsorption process onto functionalized TMAC–silica of cubic *Pm*3*n* HOM-9 monoliths (a), hexagonal HOM-2 monoliths (b), and hexagonal SBA-15 powders (c) during the synthesis of different classes of nanosensors.

The measured uptake of the PR chromophore moieties revealed that these moieties effectively appended to the nanoscale structures, as evidenced by the larger quantity of adsorption (Q; Table 1). Figure 2A shows the absorption spectra at 535 nm of the functionalized PR-probe mesostructures. The functionalized TMAC cage cubic *Pm*3*n* (HOM-9) sample clearly exhibited stronger PR-probe absorption than did the functionalized TMAC hexagonal monoliths (HOM-2) and powders (SBA-15) (Figure 2Aa–c, respectively). The difference in the PR-probe absorption behavior of these nanoscale carriers reveals the significant effect of the 3D cagelike pore geometry on the efficiency of the sensing systems with these nanosensors in detecting Sb^{III} ions, as evidenced by the resultant reflectance intensity during the detection of 2 ppm Sb^{III} ions (see Figure 2Aa′–c′).

The kinetics of nanosensor design (Figure 2B) was investigated by the measured amount of adsorbed PR probe as a function of time onto the three modified TMAC mesostructures. Figure 2B clearly reveals a significant effect of the morphological particle size and 3D pore shape of the mesostructures on the efficient design of the sensing system in terms of sensitivity and rapid response time of Sb^{III}-ion detection. However, the high degree of PR-probe accessibility and the fast kinetic diffusion onto TMAC–silica charged carriers decreased in the following order: 3D HOM-9 $>$ 2D HOM-2 $\geq$ 2D SBA-15. This decreasing order agrees with the decrease in Sb^{III}-ion detection capability (Figure 2A).

The above results reveal the following three key findings. First, among all the materials used in this study, the 3D cage carriers showed the highest adsorption rate of the probe molecule. The functionality of the nanosensor-like sinks can be attributed to uniquely shaped cages and uniformly sized cavities (Figure 2Ac,c′).[20] Second, although the modified TMAC–SBA-15 and HOM-2 materials had similar pore geometrical shapes and structures, the TMAC–HOM-2 monoliths exhibited relatively high adsorption capacity of the PR probe (Figure 2A). The relatively high PR-probe absorptivity of HOM–TMAC compared with SBA-15 might be explained by the larger primary particle size of HOM-2 compared with that of SBA-15. In turn, the diffusive mass transport into materials with small particle size, such as hexagonal SBA-15, is rapid enough compared with the same hexagonal HOM-2 material-like monoliths (Figure 2B).[41] The large particle size of HOMs, however, led to the creation of pore-surface grains (macroscale length) that enabled grafting of a large number of probe binding sites to the pore-wall surfaces of the modified TMAC silicas. Third, the large monolithic grains might also be responsible for the comparatively lower kinetic hindrance of the metal-to-ligand binding on the pore surfaces, as evidenced by the fast response time of the HOM nanosensors (see Table 1). In conclusion, nanoscale pore geometry and particle morphology both play a role in the design of efficient, highly sensitive sensing systems for Sb^{III}-ion detection.

Colorimetric and visual detection of Sb^{III} metal ions: Although, in general, the successful design of optical sensors based on nanostructures enabled the selective and sensitive detection of Sb^{III} ions down to subnanomolar concentrations (Table 1), the high performance of the sensors depended on key factors, such as the amount of support-based sensor, reaction temperature,[43] and pH.[44] However, these factors strongly affected the homogeneity in the color-map distribution and intensity (Figure 3), even at low loading levels of Sb^{III} ion during the visual detection process (see the Supporting Information S6). In general, changes in these key factors can play significant roles in the redistribution of the charge polarity and the electron and energy transfer within the probe molecule into the pore surfaces. Therefore, the chemical sensing system is extremely sensitive to such changes, which, in turn, acutely affects the accuracy and precision in the determination and visual detection of the target ions.[44] Successful visual detection of Sb^{III} ions in a wide concentration range of 0.5 ppb to 3 ppm was clearly achieved by using the nanosensors. The color of the nanosensors changed from light orange to magenta with increasing Sb^{III}-ion concentration (Figure 3A). The color reaction was stable, and no elution of the probe molecules occurred with the addition of the analyte ions. The rapid, sensitive detection of Sb^{III} at nanomolar concentrations by using the naked eye without any instrumentation (Figure 3A) indicated the high performance and reliability of this sensing system.

The UV/Vis absorption spectroscopy of PR-probe indicator in solution showed a strong metal-to-ligand charge-transfer band at 520 nm ($\varepsilon = 2.5 \times 10^3\ \text{M}^{-1}\,\text{cm}^{-1}$) by the addition of Sb^{III} target ions at pH 3.[45] The absorption intensity (data not shown) increased with increasing Sb^{III} concentration from 0.1 to 3 ppm. Key to the success of our nanosensors is the fact that colorimetric determination by UV/Vis reflectance spectroscopy could quantitatively validate the wider detection range (D_R) of the Sb^{III} ions (4.1×10^{-9} to $2.05 \times 10^{-5}\ \text{mol}\,\text{dm}^{-3}$) compared with Sb^{III}-ion recognition in solution (Table 1). However, in general, the reflection band of the PR-probe nanosensors showed a hyperchromic effect at 532 nm upon the addition of Sb^{III} ions, indicating the formation of a PR probe-to-Sb^{III} charge-transfer complex (Scheme 1). This reflection intensity at 532 nm increased with increasing Sb^{III}-ion concentration (Figure 3B–D). For all mesostructured carriers used in this study, neither the wavelength of the absorption bands of the PR-probe nanosensor nor that of the $[Sb–PR]^+$ complex was influenced by changes in either pore geometry or particle morphology (Figure 3B–D).

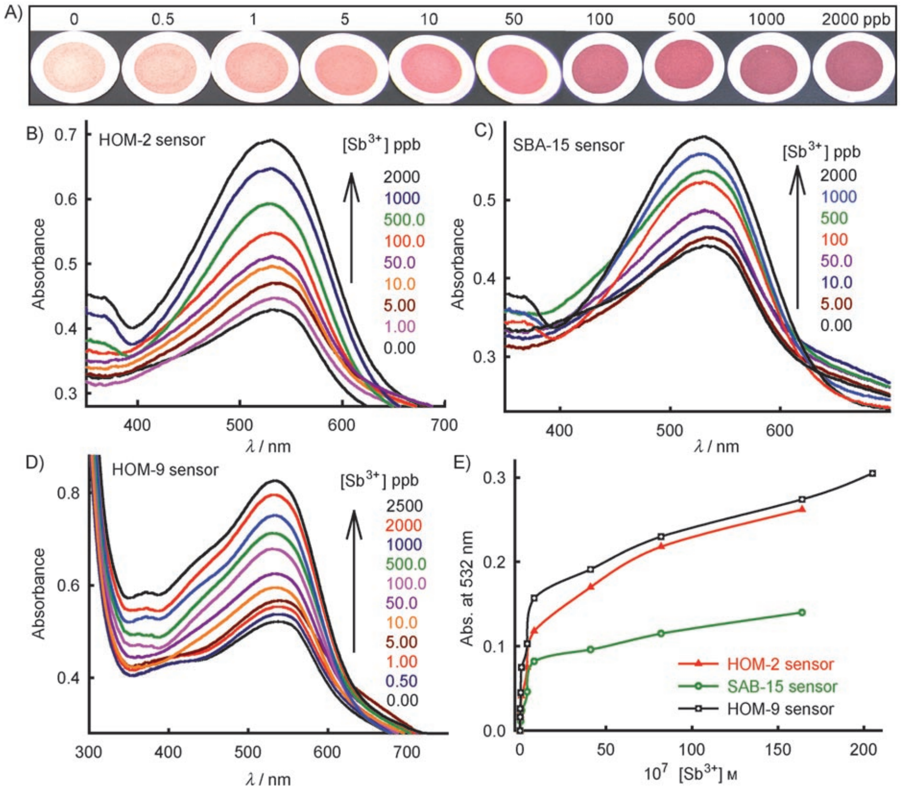

Figure 3. A) Changes in color development sequence of cage HOM-9/TMAC/PR nanosensor after detection of a wide range of concentrations of the Sb^{III} analyte ion. B–D) Concentration-dependent changes of UV/Vis absorption spectra of hexagonal nanosensor monoliths (B), hexagonal nanosensor powders (C), and cubic cage nanosensor monoliths (D) after detection of a wide range of concentrations of the Sb^{III} analyte ion at $\lambda = 532$ nm. E) Calibration curves representing the change of absorbance of the $[Sb–PR]^+$ complex at 532 nm against the Sb^{III} ion concentration.

The limit of detection (LOD) of Sb^{III} ions for the nanosensors fabricated here was estimated from the linear part of the calibration plot of the absorbance of the $[Sb–PR]^+$ complex at 532 nm against the Sb^{III}-ion concentration,[17,20] according to the equation $LOD = kS_b/m$, in which $k = 3$, S_b is the standard deviation for the blank, and m is the slope of the calibration curve in the linear range (Figure 3E). A linear correlation in the range from 0 to $3 \times 10^{-6}\ \text{M}$ was observed. At higher concentration (i.e., $\geq 3 \times 10^{-6}\ \text{M}$), the dependence is nonlinear due to saturation effects. The resultant LOD value (Table 1) indicated that the nanosensors enabled detection of Sb^{III} ions down to a concentration of $\approx 1.0 \times 10^{-9}\ \text{mol}\,\text{dm}^{-3}$. This finding indicates that the nanosensors can effectively separate and preconcentrate the Sb^{III} ions even at trace concentrations. Among all the nanosensors studied here, the immobilized PR-probe monoliths (HOM-type) were effective preconcentrators that led to higher loading and binding capacity of Sb^{III} ions in faster response times (consistent with high D_R) than those by SBA powder nanosensors (Table 1). Furthermore, the 3D HOM cage nanosensors showed an excellent sensing system in their detection range (D_R) and limit (LOD) with fast kinetic assessment (R_t). The stoichiometry of the $[Sb–PR]^+$ complex was calculated and derived from the deviation in the linearity of the calibration plot at the inflection point (Figure 3E). The stoichiometry was found to be Sb^{III}/PR 1:1 for all the nanosensors (Scheme 1), despite the change in the amount of adsorption of the PR probe with these solid nanosensors. Further evidence is provided by the fact that the stoichiometric Sb^{III}–PR reaction required 1:1 of Sb^{III}/PR, as revealed by Job's plot of the absorbance changes on formation of the $[Sb–PR]^+$ complex in solution.[45]

Advantages of the optical nanosensors

Sensing systems with fast response: The fast metal-to-ligand binding kinetics with formation of the $[Sb–PR]^+$ complex was studied by continuously monitoring the UV/Vis reflectance spectra (Figure 4) and the color change of the nanosensors after addition of Sb^{III} ions as a function of time. The results show that charge transfer between the Sb^{III} ions and PR probe occurred within a short period of time ($40\,s \leq t_R \leq 4\,min$) due to the ability of the nanostructures with large, open, uniform pore architectures to efficiently bind the Sb^{III} ions to the grafted PR probe (Figure 4). Despite the low or even high concentration of Sb^{III} ions used during the detection process, no significant change in the response time of the nanosensors was evident. The results indicated the high availability and affinity of the probe ligand for Sb^{III} binding at all metal-ion loading levels. In fact, the high metal flux, namely, ion transport, and the affinity of the metal–ligand binding were significantly affected by the mesopore shape and by the structural geometry and morphology of the fabricated nanosensors, as clearly shown by the t_R value (Table 1). This result also indicates that the cage nanosensors exhibited "sink-like" easy accessibility of Sb^{III} ions and fast Sb–PR ligand-binding events.

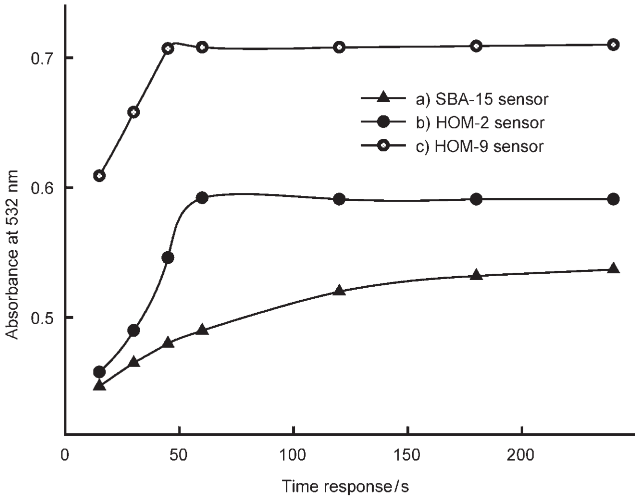

Figure 4. Influence of the structural geometry, quality, and morphology of the optical nanosensors on the kinetic response time of the sensing systems by monitoring the absorbance spectra of the $[Sb–PR]^+$ complex at $\lambda = 532$ nm with time during the detection of an Sb^{III} concentration of 500 ppb under specific sensing conditions.

Selective Sb^{III}-ion sensing systems: A major advantage of the nanoscale-structured sensors designed here is the ability to fine-tune the highly selective sensing system, when combined with actively diverse ions (interfering components) under our controlled experimental conditions. To investigate the effect of extraneous ions in the simultaneously selective detection of Sb^{III} ions, particularly at low concentrations, controlled sensing experiments were carried out in which known amounts of cations and anions were added to the Sb^{III} sensing system (Figure 5). The results showed that our sensing system for Sb^{III} target ions was affected by oppositely and potentially charged species of the interfering anions and cations. These extraneous ions can actually bind or interact with the PR-probe nanosensors, and thus these inter-

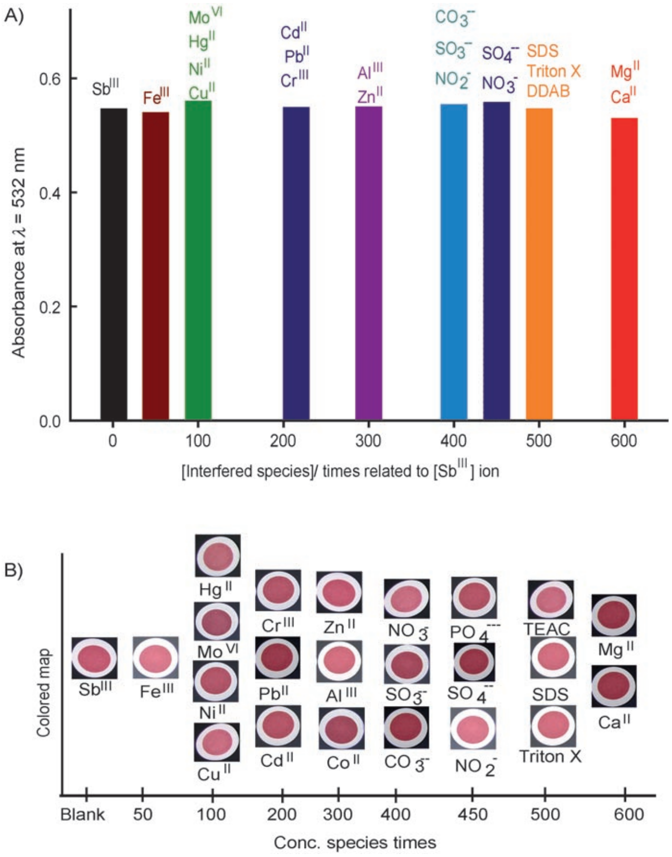

Figure 5. Illustration of the selectivity of the optical sensing system for Sb^{III} ions by studying the effect of interfering species (anions, surfactants, and cations) on A) the optical absorbance spectrum of the $[Sb–PR]^+$ complex at $\lambda = 532$ nm and B) the color density during the naked-eye detection of an Sb^{III} concentration of 100 ppb by using hexagonal nanosensor monoliths.

actions are detrimental. Despite such interactions of the extraneous ions, the optical signal of the $[Sb–PR]^+$ complex varied within a permissible tolerance limit of ±3%, indicating that the sensing system for the Sb^{III} target ions was highly tuned, functional, and selective even at nanomolar levels of detection (Table 2).[46,47]

Table 2. Illustration of the selectivity of the different nanostructured sensors within the study of the influence of the addition of a high (tolerable) concentration of diverse ions on the naked-eye detection of Sb^{III} ions [0.1 ppm] in specifically controlled sensing experiments.

Type of interfering species	Extraneous interfering ions	Tolerable concentration [ppm]			Tolerance limit[a] [%]
		Sensor structures			
		HOM-9	HOM-2	SBA-15	
cations	Ca^{II}	65	60	60	−1.3
	Mg^{II}	65	60	60	−2.2
	Co^{II}	35	30	30	−2.7
	Zn^{II}	30	30	30	−3.2
	Al^{III}	35	30	30	−2.9
	Cd^{II}	25	20	20	+2.3
	Pb^{II}	20	20	20	+2.2
	Cr^{III}	25	20	20	+3.3
	Mo^{VI}	15	10	10	+1.0
	Hg^{II}	15	10	10	+1.3
	Ni^{II}	15	10	10	+1.3
	Cu^{II}	10	10	10	+1.5
	Fe^{III}	6	5	5	−1.7
anions	NO_3^-	50	45	45	+2.2
	SO_4^{2-}	50	45	45	+1.2
	PO_4^{2-}	50	45	45	+1.5
	SO_3^{2-}	45	40	40	+1.2
	CO_3^{2-}	45	40	40	+1
	NO_2^-	40	40	40	+1
surfactants	Triton X	60	50	50	−1.0
	SDS[b]	55	50	50	−2.1
	TEAC[c]	60	50	50	+1.2

[a] Tolerance limit was estimated from the average effect of the species with all sensor types. [b] Sodium dodecyl sulfate. [c] Tetraethylammonium chloride.

No changes in either the developed color or the absorbance intensities of the $[Sb–PR]^+$ complex were observed (Figure 5), despite the addition of cations, which are effective disturbance species at a concentration 50–600 times higher than that of Sb^{III} ions. Among all possible interfering cation species, Fe^{III} ions at high concentration showed a significant change in the absorbance and color intensity of the $[Sb–PR]^+$ complex, indicating a disturbance in the Sb^{III} ion sensing system. To counteract such a disturbance, the addition of 1 mL of 1% NH_4F to the specific sensing conditions can enhance the tolerable concentration of the active Fe^{III} species. Significantly, the addition of various types of surfactants and anion species showed no interference effects, even when their concentrations were up to 500 times higher than that of Sb^{III} ions (Figure 5).

In this respect, the nanostructured PR-probe-based sensors exhibited high selectivity for the Sb^{III} target ion, thus permitting accurate, specific detection of Sb^{III} analyte ions without interference from the active-component species.[13–18] Under specific sensing conditions, two key factors affect the selectivity of the nanostructured sensing systems. First, nanostructured sensors exhibit selectivity even at low concentrations of target ions (nanomolar scale). However, active interfering species and multiple components at much higher concentrations can be introduced into these nanostructured sensors without affecting significantly either the physical characteristics or chemical properties. This retention of nanosensor features allowed an efficient binding of the multifunction components with PR probe molecules in the sensors without distortion in the formation of the octahedral $[Sb–PR]^+$ complex. Second, the 3D-ordered sensor with nanoscale open-pore arrays, high surface areas, and high pore volumes might enhance fast, homogeneous distribution of the multi-ion transport species onto the modified PR probe, leading to a durable signal as a response to the Sb^{III}–PR probe binding event. Evidence of such selectivity and performance of Sb^{III}-ion sensing systems is indicated by the data for 3D HOM-9 nanosensors summarized in Tables 1 and 2.

Stability of the nanosensors: The stability of the grafted PR-probe-based nanosensors was examined for 2D and 3D mesostructured traps. Long-term retention of the electron acceptor/donor strength of the probe functional group makes the optical sensing systems technologically promising.[17,20] In our developed sensor-based nanostructured materials, the robustness in the sensor design involving silica–TMAC–PR construction provided control over the potential leaching of the hydrophilic PR chromophore upon washing cycles or after long-term storage (Table 1). However, the strong electrostatic interactions (Coulombic type) of the hydrophilic PR probe with charged surfaces grafted by the TMAC ligand led to stable, confined sensors. Our results show that only a slight change in the optically colored density of the "absorption spectra" for the PR probe was evident even after long-term storage (on the order of months), further evidence of efficient sensing functionality.

Table 1 summarizes the deactivation "degradation" behavior of the specific activity of the probe functional group with the different nanostructure-based sensors, including 2D hexagonal *P6mm* powders (SBA-15) and monoliths (HOM-2), and 3D cage cubic monoliths (HOM-9). The findings indicate that the stability of the nanosensors was substantially influenced by the structural characteristics of the mesostructured carriers, namely, morphology, geometry, and pore shape. Among these nanostructured PR-probe sensors, the more active site probes in the meso/macroporous pore surfaces of monoliths were more effectively utilized in the sensing of Sb^{III} ions for a longer time than in the SBA-15 powders (Table 1). These results, in principle, revealed the beneficial effect of the large-particle morphology of free-supporting monoliths as a result of their open macroporous pores with fractal connectivity networks that yielded much higher probe loading and trapping levels. Both the structural characteristics and the high adsorption capacity were responsible for the retention of active functions of probe indicators during long-term storage. Among all the nanosensors designed here, the HOM-9 cage nanosensor showed higher stability due to the interior cavities of the cage-pore connectivity acting as retaining probe sinks.[20] The design of an optical nanosensor that is based on appropriately tailored nanostructures by tuning the surface characteristics with charge-carrier groups enables the sensing systems to achieve long-term stability in their functionalities, despite the longer storage time (Table 1). Such long-term stability makes these sensing systems particularly applicable to detection of other toxic metal ions.[1–3]

Reversibility of the Sb^{III}-ion sensing systems: A major advantage of the nanostructured sensors is their retained functionality in terms of sensitivity with fast response time even after multiple regeneration/reuse cycles of the $[Sb–PR]^+$ complexes in the materials.[1–3,20] Although improvement of the reducibility and reversibility of the chemical sensors is a challenge, the nanostructured sensor can extend control of the Sb^{III}-ion detection even after several cycles of decomplexation in which an appropriate stripping agent is used, such as 0.01 M EDTA (Scheme 1). After multiple regeneration/reuse cycles (i.e., ≥ 3), although the regenerated nanosensors showed a relatively lower sensitivity with higher metal-to-ligand kinetic hindrances, they also showed well-controlled signaling in the visual detection (see Table 1).

As a consequence of the recycle process, the effective binding and signaling of the metal-ion targets to the probe functional sites might become significantly degraded due to the substantial influence of the stripping agent (EDTA) upon cycling. Elemental analyses (data not shown) confirmed that the number of probe molecules adsorbed onto the silica surfaces decreased after each regeneration cycle, indicating the severe detrimental effect of the stripping agent on the nanosensor design. The extent of this effect depended on the probe–TMAC interaction strength, grain particle size, and pore geometry. For the regenerated SBA-15 powder sensor, the decrease in sensing functionality in terms of sensitivity and response time was much greater and more rapid than that for either hexagonal or cubic monolith-based sensors. The SBA-15 powder sensor lost about 15% of its original sensing efficiency after only a single regeneration/reuse cycle, whereas the monolithic sensors lost the same amount after three reuse cycles. Although the time response of such regenerated sensors was generally influenced by the extensive cycling process, the binding and signaling remained relatively fast, on the order of minutes, and fully revisable.[46–48]

To understand the differences in the sensing efficiency among the various regenerated nanosensors, textural parameters were examined for all the nanostructured sensors after the reuse cycles (Table 1). The results revealed that all of the sensing systems experienced a significant reduction in surface area and pore volume, in particular. Compared to the SBA powder sensors, the meso/macroporous surfaces of monolith-based nanosensors showed higher reversibility due to the open interconnectivity of the macropore grains. These large pore-surface grains might induce high adsorption characteristics of the probe and accessibility for analyte ion transport, thus leading to the retention of a large amount of probe. This loading amount of probe can act as a selective sensor with highly efficient sensitivity without much higher kinetic hindrance, despite the slight potential of leaching of the probe from the pore surface during the decomplexation process. The nanosensors thus achieve high performance and are therefore highly applicable to environmental cleanup of toxic heavy-metal ions.

Conclusion

The manipulation of matter at the nanoscale level led to new frontiers in nanotechnology and materials science, including the development of optical nanosensors. As a consequence, the nanostructured sensors designed in this study exhibited interesting selective behavior that permits accurate, specific detection of Sb^{III} analyte ions down to nanomolar concentrations with rapid response times. The robustness within the nanosensor design involving silica–TMAC–PR construction provided control over the potential leaching of the hydrophilic PR chromophore probe during washing cycles or even after long-term storage (in the order of months). Although optimizing the reducibility and reversibility of the chemical sensors remains a unique and interesting challenge, these nanostructured sensors can extend the control of Sb^{III}-ion detection even after several regeneration cycles of the decomplexation process. In general, the 2D- and 3D-ordered sensor structures with nanoscale monoliths, open-pore arrays, high surface area, and high pore volume might enhance fast and homogeneous distribution of the multi-ion transport species onto the sensor pore surfaces, leading to the selectivity the Sb^{III}-ion sensing systems. Among all materials used in this study, the 3D cage HOM nanosensor-like sinks with uniquely shaped cages and uniformly sized cavity showed the highest sensing functionality in terms of sensitivity and rapid response time of Sb^{III} ion detection, indicating the significant effect of the 3D pore shape of the mesostructures on the efficient design of the sensing system. In general, the current study revealed the advantages of nanoscale pore geometry and shape, and particle morphology of the support carriers, in the design of optical nanosensors that can efficiently and accurately enhance the Sb^{III}-ion sensing functionality in terms of sensitivity and detection response time. Such integration of nanosensors is the key to further development of visual detection with high performance for environmental cleanup of toxic heavy-metal ions.

Experimental Section

Materials: All chemicals used were of analytical reagent (AR) grade and used as purchased without further purification. Tetramethylorthosilicate

(TMOS), tetraethylorthosilicate (TEOS), triblock copolymer Pluronic P123 ($EO_{20}PO_{70}EO_{20}$), Brij 56 (polyoxyethylene, $C_{16}H_{33}(OCH_2CH_2)_{10}OH$, $C_{16}EO_{10}$), and dodecane (C_{12} alkane) were obtained from Sigma–Aldrich (USA). Anhydrous ethanol and toluene were purchased from Wako (Japan). *N*-Trimethoxysilylpropyl-*N*,*N*,*N*-trimethylammonium chloride (TMAC) (50 % methanol solution) and Pyrogallol Red (PR) were purchased from Gelest (Japan).

Design of mesostructured PR-carrier nanosensors: High-quality structures with uniformly packed arrays arranged into hexagonal mesochannels of powdery SBA-15 and monolithic HOM-2 materials were successfully fabricated by using P123 ($EO_{20}PO_{70}EO_{20}$) and Brij 56 ($C_{16}EO_{10}$) templates in acidic conditions, as previously reported.[28,29] In addition, through hexagonal *P6mm*–cubic *Pm*3*n* phase transition (see the Supporting Information S1), cubic *Pm*3*n* mesophase structures (HOM-9) were fabricated by using instant direct-templating of microemulsion liquid crystals of Brij 56 with C_{12} alkane as a co-solvent.[30] The calcined mesostructured materials were firstly anchored by a grafting technique via the TMAC ligand in refluxing toluene for 24 h at 90–100 °C. The grafted materials were then washed with ethanol and methylene chloride, and dried under vacuum at 80 °C for 5 h. The immobilization of PR probe molecules with silica–TMAC was achieved by adding aqueous solutions of these probes (10 mg/100 mL H_2O) to 1.0 g silica–TMAC solids under stirring for 5 h. The immobilized PR probe was thoroughly washed by using deionized water several times until no color was observed. The resulting silica–TMAC–PR sensor was dried at 65 °C for 2 h and then ground to a fine powder (100 µm-diameter particles), particularly when applying HOM carriers, before being used for Sb^{III} detection. In general, the adsorption amounts (*Q*) of the probe molecules at the saturation "equilibrium" step were determined by monitoring the absorbance spectra of the probe with respect to the adsorption time during the synthesis of the nanosensor designs.

Colorimetric recognition of Sb^{III} ions by nanosensors: Different concentrations of Sb^{III} solution, ranging from 0.5 ppb to 3 ppm at pH 3.0 (adjusted with 0.2 M KCl/HCl), were added to solid nanosensors (4 mg) at a constant volume of 20 cm^3 at room temperature. After a given interval of time (0.5–4 min) depending on the nature of the sensing systems, the solid sensor materials were collected by suction using 25 mm cellulose acetate filter paper (Sibata filter holder). The color of each collected sample was estimated qualitatively by visual inspection and quantitatively by UV/Vis spectrometry at 532 nm. The absorbance intensity of collected nanosensor samples of the Sb^{III} target was compared with that of standard Sb^{III} samples to calculate the concentration of Sb^{III} target ions. Note that the effect of pH on the colorimetric detection of Sb^{III} ions was studied by adding a mixture containing a specific concentration of Sb^{III} ions adjusted to a pH of 1–3 (by using 0.2 M KCl/HCl), 4–6 (by using 0.2 M CH_3COOH/CH_3COONa), 7–8 (by using 0.2 M 3-morpholinopropanesulfonic acid, MOPS), and 9–11 (by using 0.2 M 2-cyclohexylaminoethanesulfonic acid, CHES) under the same conditions. Results from this pH study showed that the maximum absorbance intensity of the metal–ligand (Sb^{III}–PR) complex was exhibited at pH 3.0. The pH was measured by using a Horiba digital pH meter with a glass electrode.

Analyses: The metal-ion concentration was determined by using a Seiko SPS-1500 ICP atomic-emission spectrometer. The absorbance spectrum of the solid material was recorded with a UV/Vis spectrometer (Shimadzu 3150, Japan). Small-angle powder XRD patterns were measured by using an MXP 18 diffractometer (Mac Science) with monochromated $Cu_{K\alpha}$ radiation. The textural surface properties of the solid carrier and nanosensor materials, such as the specific surface area and pore structure, were determined by measuring the N_2 adsorption/desorption isotherms at 77 K with a BELSORP36 analyzer (BEL, Japan). Specific surface area (S_{BET}) was calculated by using multipoint adsorption data from the linear portion of the N_2 adsorption isotherms based on the Brunauer–Emmett–Teller (BET) theory. The pore size distribution was then determined from the adsorption curve of the isotherms by using nonlocal density functional theory (NLDFT). Before this N_2 isothermal analysis, all samples were pretreated at 100–200 °C for 8 h under vacuum until the pressure was equilibrated to 10^{-3} Torr. Energy-dispersive X-ray microanalysis (DS-130S) was used to determine the elemental composition of the nanosensor materials. FTIR spectra were recorded by using an FTIR Prestige-21 spectrometer (Shimadzu, Japan). TGA and DTA were performed with a Thermo Plus TG8120 apparatus (Rigaku, Japan). TEM images were obtained by using a JEOL microscope (JEM-2000EXII) operated at 200 kV with a side-mounted CCD camera (Mega View III, Soft Imaging System). ^{29}Si magic-angle spinning NMR spectra were also measured at room temperature by using a Bruker AMX-500 spectrometer operated at 125.78 MHz with a 90° pulse length of 4.7 µs. For all samples, the repetition delay was 180 s with rotor spinning at 4 kHz.

Acknowledgements

The authors thank the Japan Society for the Promotion of Science (JSPS) for financial support of this project.

[1] a) J.-M. Nam, C. S. Thaxton, C. A. Mirkin, *Science* **2003**, *301*, 1884; b) R. Elghanian, J. J. Storhoff, R. C. Mucic, R. L. Letsinger, C. A. Mirkin, *Science* **1997**, *277*, 1078; c) F. Turner, *Science* **2000**, *290*, 1315; d) P. Chen, C. He, *J. Am. Chem. Soc.* **2004**, *126*, 728.

[2] a) R. A. Potyrailo, *Angew. Chem.* **2006**, *118*, 718; *Angew. Chem. Int. Ed.* **2006**, *45*, 702; b) O. S. Wolfbeis, *J. Mater. Chem.* **2005**, *15*, 2657.

[3] a) M. Boiocchi, M. Bonizzoni, L. Fabbrizzi, G. Piovani, A. Taglietti, *Angew. Chem.* **2004**, *116*, 3935; *Angew. Chem. Int. Ed.* **2004**, *43*, 3847; b) B. Lei, B. Li, H. Zhang, S. Lu, Z. Zheng, W. Li, Y. Wang, *Adv. Funct. Mater.* **2006**, *16*, 1883.

[4] a) M. M. Henary, C. J. Fahrni, *J. Phys. Chem. A* **2002**, *106*, 5210; b) J. Homola, S. S. Yee, G. Gauglitz, *Sens. Actuators B* **1999**, *B54*, 3.

[5] a) H.-A. Ho, M. Leclerc, *J. Am. Chem. Soc.* **2004**, *126*, 1384; b) C. Zhang, K. S. Suslick, *J. Am. Chem. Soc.* **2005**, *127*, 11548.

[6] a) M. J. E. Resendiz, J. C. Noveron, H. Disteldorf, S. Fischer, P. J. Stang, *Org. Lett.* **2004**, *6*, 651; b) T. Mayr, C. Igel, G. Liebsch, I. Klimant, O. S. Wolfbeis, *Anal. Chem.* **2003**, *75*, 4389.

[7] C. Hagleitner, A. Hierlemann, O. Brand, H. Baltes, *Sensors Update, Vol. 11*, Wiley-VCH, Weinheim, **2002**, pp. 101–155.

[8] P. T. Hammond, *Adv. Mater.* **2004**, *16*, 1271.

[9] A. B. Desacalzo, K. Rurack, H. Weisshoff, R. M. Manez, M. D. Marcos, P. Amoros, K. Hoffmann, J. Soto, *J. Am. Chem. Soc.* **2005**, *127*, 184.

[10] a) J. Liu, Y. Lu, *J. Am. Chem. Soc.* **2004**, *126*, 12298; b) E. Coronado, J. R. Galàn-Mascarós, C. Marti-Gastaldo, E. Palomares, J. R. Durrant, R. Vilar, M. Grätzel, Md. K. Nazeeruddin, *J. Am. Chem. Soc.* **2005**, *127*, 12351.

[11] a) S. Deo, H. A. Godwin, *J. Am. Chem. Soc.* **2000**, *122*, 174; b) M. Rex, F. E. Hernandez, A. D. Campiglia, *Anal. Chem.* **2006**, *78*, 445; c) C. C. Woodroofe, S. J. Lippard, *J. Am. Chem. Soc.* **2003**, *125*, 11458.

[12] a) M. Comes, G. Roríguez-López, M. D. Marcos, R. M. Martínez-Mánez, F. Sancenón, J. Soto, L. A. Villaescusa, P. Amorós, D. Beltrán, *Angew. Chem.* **2005**, *117*, 2978; *Angew. Chem. Int. Ed.* **2005**, *44*, 2918; b) M. Comes, M. D. Marcos, F. Sancenón, J. Sato, L. A. Villaescusa, P. Amorós, D. Beltrán, *Adv. Mater.* **2004**, *16*, 1783; c) X. Li, S. M. Husson, *Langmuir* **2006**, *22*, 9658.

[13] a) E. Palomares, R. Vilar, J. R. Durrant, *Chem. Commun.* **2004**, 362; b) E. Palomares, R. Vilar, A. Green, J. R. Durrant, *Adv. Funct. Mater.* **2004**, *14*, 111.

[14] L. Nicole, C. Boissiere, D. Grosso, P. Hesemann, J. Moreau, C. Sanchez, *Chem. Commun.* **2004**, 2312.

[15] R. Metivier, I. Leray, B. D. Lebeau, B. Valeur, *J. Mater. Chem.* **2005**, *15*, 2965.

[16] J. Shi, Y. Zhu, X. Zhang, W. R. G. Baeyens, A. M. Garcia-Campana, *TrAC Trends Anal. Chem.* **2004**, *23*, 351.

[17] a) T. Balaji, M. Sasidharan, H. Matsunaga, *Anal. Bioanal. Chem.* **2006**, *384*, 488; b) T. Balaji, M. Sasidrharan, H. Matsunaga, *Analyst* **2005**, *130*, 1162; c) N. A. Carringto, G. H. Thomasa, D. L. Rodmana, D. B. Beach, Z.-L. Xue, *Anal. Chim. Acta* **2007**, *581*, 232.

[18] a) S. O. Obare, R. E. Hollowell, C. J. Murphy, *Langmuir* **2002**, *18*, 10407; b) G. Wirnsberger, B. J. Scott, G. D. Stucky, *Chem. Commun.* **2001**, *1*, 119; c) G. J. Mohr, *Anal. Bioanal. Chem.* **2006**, *386*, 1201.

[19] a) X. Feng, G. E. Fryxell, L. Q. Wang, A. Y. Kim, J. Liu, K. M. Kemner, *Science* **1997**, *276*, 923; b) L. Mercier, T. J. Pinnavaia, *Environ. Sci. Technol.* **1998**, *32*, 2749; c) L. Mercier, T. J. Pinnavaia *Adv. Mater.* **1997**, *9*, 500.

[20] S. A. El-Safty, T. Balaji, H. Matsunaga, T. Hanaoka, F. Muzukami, *Angew. Chem.* **2006**, *118*, 7360; *Angew. Chem. Int. Ed.* **2006**, *45*, 7202.

[21] a) L. H. Keith, W. A. Telliard, *Environ. Sci. Technol.* **1979**, *13*, 416; b) M. Dodd, S. A. Pergantis, W. R. Cullen, H. Li, G. K. Eigendorf, K. J. Reimer, *Analyst* **1996**, *121*, 223; c) M. Filella, N. Belzile, Y. Chen, *Earth-Sci. Rev.* **2002**, *57*, 125.

[22] a) M. O. Andreae, J. F. Asmode, P. Foster, L. Van't Dack, *Anal. Chem.* **1988**, *53*, 1766; b) H. Onishi, E. B. Sandell, *Geochim. Cosmochim. Acta* **1955**, *8*, 213; c) X. Lu, J. Li, S. Chen, D. Guosheng, *Acta Oceanol. Sinica* **1990**, *9*, 255.

[23] M. Krachler, H. Emons, J. Zheng, *TrAC Trends Anal. Chem.* **2001**, *20*, 79.

[24] a) N. Ozdemir, M. Soylak, L. Elci, M. Dogan, *Anal. Chim. Acta* **2004**, *505*, 37; b) M. Yu, G. Liu, *Talanta* **1983**, *30*, 265; c) Y. C. Sun, J. Y. Yang, *Anal. Chim. Acta* **1999**, *395*, 293.

[25] a) S. Garbos, E. Bulska, A. Hulanicki, Z. Fijalek, K. Soltyk, *Spectrochim. Acta Part B* **2000**, *55*, 793; b) L. A. Trivelin, J. J. Rodrigues, S. Rath, *Talanta* **2006**, *68*, 1536; c) A. P. Waller, W. F. Pickering, *Talanta* **1995**, *42*, 197.

[26] a) A. Erdem, A. Eroglu, *Talanta* **2005**, *68*, 86; b) J. Y. Cabon, C. L. Madec, *Anal. Chim. Acta* **2004**, *504*, 209.

[27] a) I. Gregori, W. Quiroz, H. Pinochet, F. Pannier, M. Potin-Gautier, *J. Chromatogr. A* **2005**, *1091*, 94; b) P. Montesinos, M. L. Cervera, A. Pastor, M. Guardia, *Talanta* **2003**, *60*, 787; c) S. Sato, *Talanta* **1985**, *32*, 341.

[28] a) S. A. El-Safty, T. Hanaoka, *Chem. Mater.* **2003**, *15*, 2892; b) S. A. El-Safty, T. Hanaoka, *Adv. Mater.* **2003**, *15*, 1893.

[29] D. Zhao, J. Feng, Q. Huo, N. Melosh, G. H. Fredrickson, B. F. Chmelka, G. D. Stucky, *Science* **1998**, *279*, 548.

[30] S. A. El-Safty, T. Hanaoka, *Chem. Mater.* **2004**, *16*, 384.

[31] H. G. Chen, J. L. Shi, H. R. Chen, Y. S. Li, Z. L. Hua, D. S. Yan, *Appl. Phys. B* **2003**, *77*, 89.

[32] a) Z. Yan, G. Li, L. Mu, S. Tao, *J. Mater. Chem.* **2006**, *16*, 1717; b) Q. Wei, Z.-R. Nie, Y.-L. Hao, L. Liu, Z.-X. Chen, J.-X. Zou, *J. Sol-Gel Sci. Technol.* **2006**, *39*, 103.

[33] a) K. Nakajima, I. Tomita, M. Hara, S. Hayashi, K. Domen, J. N. Kondo, *J. Mater. Chem.* **2005**, *15*, 2362; b) X. Ji, Q. Hu, J. E. Hampsey, X. Qiu, L. Gao, J. He, Y. Lu, *Chem. Mater.* **2006**, *18*, 2265.

[34] a) G. Engelhardt, D. Michel, *High Resolution Solid-State NMR of Silicates and Zeolites*, Wiley, New York, **1987**; b) M. Magi, E. Lippmaa, A. Samoson, G. Engelhardt, A. R. Grimmer, *J. Phys. Chem.* **1984**, *88*, 1518; c) J. M. Maher, N. J. Cooper, *J. Am. Chem. Soc.* **1980**, *102*, 7606.

[35] a) C. W. Clavier, D. L. Rodman, J. F. Sinski, L. R. Allain, H.-J. Im, Y. Yang, J. C. Clark, Z.-L. Xue, *J. Mater. Chem.* **2001**, *15*, 2356; b) A. Liu, M. K. Hidajat, S. Kawi, D. Y. Zhao, *Chem. Commun.* **2000**, 1145; c) Y.-H. Liu, H.-P. Lin, C.-H. Mou, *Langmuir* **2004**, *20*, 3231.

[36] a) Q. Huo, D. Margolese, U. Ciesla, P. Feng, T. E. Gier, P. Sieger, R. Leon, P. M. Petroff, F. Schüth, G. D. Stucky, *Nature* **1994**, *368*, 317; b) Y. Sakamoto, M. Kaneda, O. Terasaki, D. Y. Zhao, J. M. Kim, G. D. Stucky, H. J. Shin, R. Ryoo, *Nature* **2000**, *408*, 449; c) A. E. Garcia-Bennett, K. Lund, O. Terasaki, *Angew. Chem.* **2006**, *118*, 2494; *Angew. Chem. Int. Ed.* **2006**, *45*, 2434.

[37] a) M. Kruk, M. Jaroniec, C. H. Ko, R. Ryoo, *Chem. Mater.* **2000**, *12*, 1961; b) P. I. Ravikovitch, A. V. Neimark, *J. Phys. Chem. B* **2001**, *105*, 6817.

[38] a) J. R. Matos, M. Kruk, M. Jaroniec, L. Zhao, T. Kamiyama, O. Terasaki, T. J. Pinnavaia, Y. Liu, *J. Am. Chem. Soc.* **2003**, *125*, 821; b) B. N. Newalkar, S. Komarneni, U. T. Turaga, H. Katsuki, *J. Mater. Chem.* **2003**, *13*, 1710.

[39] a) M. Kruk, M. Jaroniec, *Chem. Mater.* **2003**, *15*, 2942; b) P. I. Ravikovitch, A. V. Neimark, *Langmuir* **2002**, *18*, 1550.

[40] a) L. Feng, Z. Chen, D. Wang, *Spectrochim. Acta Part A* **2007**, *66*, 599; b) C. Yang, Y. Wang, B. Zibrowius, F. Schüth, *Phys. Chem. Chem. Phys.* **2004**, *6*, 2461.

[41] J. J. Chiu, D. J. Pine, S. T. Bishop, B. F. Chmelka, *J. Catal.* **2004**, *221*, 400.

[42] a) M. Nappa, J. S. Valentine, *J. Am. Chem. Soc.* **1978**, *100*, 5075; b) N. A. Rakow, K. S. Suslick, *Nature* **2000**, *406*, 712.

[43] a) S. A. El-Safty, *J. Colloid Interface Sci.* **2003**, *260*, 184; b) A.-S. Chauvin, J.-C. G. Bunzli, F. Bochud, R. Scopelliti, P. Froidevaux, *Chem. Eur. J.* **2006**, *12*, 6852.

[44] a) J. Liu, Y. Lu, *J. Am. Chem. Soc.* **2004**, *126*, 12298; b) J. Liu, Y. Lu, *Anal. Chem.* **2004**, *76*, 1627; c) T. Umemura, H. Hotta, T. Abe, Y. Takahashi, H. Takiguchi, M. Uehara, T. Odake, K. Tsunoda, *Anal. Chem.* **2006**, *78*, 7511; d) M. K. Nazeeruddin, D. D. Censo, R. Humphry-Baker, M. Grätzel, *Adv. Funct. Mater.* **2006**, *16*, 189.

[45] a) K. L. Cheng, K. Ueno, T. Imamura, *CRC Handbook of Organic Analytical Reagents*, CRC Press, Boca Raton, Florida, **1982**, p. 50; b) L. Naruskevadus, R. Kazlauskas, J. Skadauskas, N. Karitonaite, *Nauch. Tr. Vyssh. Uchebn. Zaved. Lit. SSR Khim. Teknol.* **1972**, 95; c) *Anal. Abstr.* **1974**, *26*, 2616.

[46] D. S. Koktysh, X. R. Liang, B. G. Yun, I. Pastoriza-Santos, R. L. Matts, M. Giersig, C. Serra-Rodriguez, L. M. Liz-Marzan, N. A. Kotov, *Adv. Funct. Mater.* **2002**, *12*, 225.

[47] a) R. Krämer, *Angew. Chem.* **1998**, *110*, 804; *Angew. Chem. Int. Ed.* **1998**, *37*, 772; b) M. Schmittel, H.-W. Lin, *Angew. Chem.* **2007**, *119*, 911; *Angew. Chem. Int. Ed.* **2007**, *46*, 893.

[48] a) M. J. Manos, C. D. Malliakas, M. G. Kanatzidis, *Chem. Eur. J.* **2007**, *13*, 51; b) L. Feng, Z. Chen, *Sens. Actuators B* **2007**, *122*, 600.

Received: March 30, 2007